





Denosing of Dynamic Contrast-enhanced Ultrasound Sequences: A Multilinear Approach

Metin Calis¹^a, Massimo Mischi²^b, Alle-Jan Van Der Veen¹^c and Borbála Hunyadi¹^d

¹*Faculty of Electrical Engineering, Mathematics and Computer Science, Delft University of Technology, 2628 CD Delft, The Netherlands*

²*Department of Electrical Engineering, Eindhoven University of Technology, 5600 MB Eindhoven, The Netherlands*

Keywords: Multilinear Singular Value Decomposition, Dynamic Contrast-enhanced Ultrasound, Prostate Cancer, Tensor Decomposition.

Abstract: The recent advances in three-dimensional imaging of contrast-enhanced ultrasound acquisitions enable the characterization of the tissue with a single intravenous injection of microbubbles. Many cancer markers have been extended to cover for the three-dimensional contrast ultrasound. However, most of the signal denosing algorithms do not exploit the added dimensionality and vectorize the spatial dimensions, causing a loss of information about the location of the voxels. This paper proposes a denosing algorithm based on the multilinear singular value decomposition and compares it to the singular value decomposition. The ranks are estimated based on information-theoretic criteria, and improved performance has been observed for modeling the time-intensity curves.


1 INTRODUCTION


Prostate cancer (PCa) is found to be the most common malignancy among American men except for skin cancer, and according to the estimates for 2021, 248,530 new cases are expected of which 34,130 people will die from the disease (Siegel et al., 2021). The recommended guidelines for detection and grading of PCa is ≥ 10 -core systematic biopsy (Mottet et al., 2017), which consists of an invasive procedure that can still miss significant PCa lesions (Ukimura et al., 2013). In addition, infectious complications might arise due to the insertion of needles through the rectal wall (Loeb et al., 2013). Also, because of the poor patient selection by prostate specific antigen blood testing, about 3 of 4 biopsies are in retrospect unnecessary, as no cancer is found. Recent advances in imaging techniques can potentially reduce the needle-cores in systematic biopsy and overcome unnecessary biopsies (Elwenspoek et al., 2019).


One of the featured techniques to classify PCa is the detection of angiogenesis, which is the rapid


growth of new blood vessels around the tumorous region. The newly formed capillaries create a tortuous and a highly irregular network, that can be analyzed by modelling the flow dynamics of the ultrasound contrast agents (UCAs) (Seitz et al., 2009) (Russo et al., 2012). Although several modalities have been proposed that can monitor the UCAs, we focus on dynamic contrast-enhanced ultrasound (DCEUS) because of the promising results for PCa localization (Liu et al., 2020) (Wildeboer et al., 2019). In DCEUS, contrast agents that are smaller than $10 \mu\text{m}$ are imaged using a low energy ultrasound pulse. The frequency of the pulse is around the resonance frequency of the UCAs, which enhances the contrast between the microbubbles and the surrounding tissue. The time-intensity curves (TICs) of these contrast agents correlates with the underlying vasculature (Strouthos et al., 2010), which can be exploited to classify PCa.

There has been a substantial amount of work in the analysis of the perfusion characteristics of TICs (Eckersley et al., 2002) (Elie et al., 2007). Although increased perfusion is expected due to the increased microvascular density, contradictory effects of angiogenesis and perfusion have been observed (Gillies et al., 1999). The flow resistance might reduce due to the introduction of arteriovenous shunts and lack of vasomotor control. This effect might

^a <https://orcid.org/0000-0002-7576-6647>

^b <https://orcid.org/0000-0002-1179-5385>

^c <https://orcid.org/0000-0003-4249-585X>

^d <https://orcid.org/0000-0002-9333-9024>

not be observed due to the small diameter of the newly formed microvessels and the increased interstitial pressure because of the extravascular leakage (DeLorme and Knopp, 1998). A different path has been taken by (Mischi et al., 2009) (Mischi et al., 2003) where the authors have modeled the multi-trajectory bubble transport inside the prostate as a convective-dispersion process and introduced a new model based on dispersion characteristics, namely the modified local density random walk model (mLDRW) (Kuenen et al., 2011). The authors have reported a good correlation between dispersion and angiogenesis even though the single-dimensional TICs suffer from a low signal-to-noise (SNR) ratio.

Several techniques were proposed to remove the noise of various origins from the DCEUS signals. Spatial filters were used to denoise the speckle noise (Bar-Zion et al., 2015) (Joel and Sivakumar, 2018), temporal filters were proposed to denoise the clutter (Bjaerum et al., 2002). These methods assumed that the temporal and spatial frequency of the desired signal and the noise were different. Using a different approach, the authors at (Wildeboer et al., 2020) proposed the blind source separation (BSS) of the DCEUS recording into sources where the desired signal was recovered by discarding the noise sources. The best performing BSS was found to be singular value decomposition (SVD) for modelling of the time intensity curves. The dynamics of the UCAs have been captured in the first few singular values of the decomposition. Although several cancer markers such as the similarity between TICs (Schalk et al., 2015a) and solutions to convective dispersion models (Wildeboer et al., 2018b) (Wildeboer et al., 2018a) have been extended to 3D, the denoising algorithms do not take the multidimensional structure of the recording into consideration.

The SVD denoising analyzed by (Wildeboer et al., 2020) creates the Casorati matrix, which vectorizes the spatial dimension into rows and the temporal dimension into columns. The vectorization of the spatial dimension into rows results in a loss of spatial information regarding the location of the voxels. The multilinear singular value decomposition (MLSVD) proposed by (De Lathauwer et al., 2000) keeps the tensor format of the data and generalizes the concept of SVD to multiple dimensions. The information that is retained by keeping the tensor format of the data is hypothesized to enable a better representation of the bubble dynamics and hence, a better denoising capability. The MLSVD has been applied for clutter filter denoising in power Doppler images (Zhu et al., 2020) (Ozgun and Byram, 2020). Improved sensitivity and specificity have been observed. As far as the authors'

knowledge, there has not been any work done in analyzing the performance of MLSVD in TIC dispersion modeling. This paper aims to answer the following research question: Can the retained 3D structural information provided by MLSVD improve the classification performance of TIC dispersion modeling compared to SVD?

2 BACKGROUND INFORMATION

In this section, the notation is introduced and the multilinear singular value decomposition (MLSVD) is explained.

2.1 Notation

The tensor notation of (De Lathauwer et al., 2000) is adapted in this paper. Tensors are represented with calligraphic letters, for example, \mathcal{Y} and \mathcal{G} . The matrices are represented with bold face letters, for example, $\mathbf{U}^{(1)}$ and \mathbf{V} . Here, the numbers given as superscripts in parenthesis are used to refer to the different matrices, that share a similar property. An example could be the n -mode factor matrices of the same decomposition, which will be explained in the following subsection. The scalars are represented with lower case letters, such as, $(\mathbf{A})_{ij} = a_{ij}$ and $(\mathbf{U})_{i_1 i_2 i_3} = u_{i_1 i_2 i_3}$. The subscripts refer to the indices in different modalities. For example, a_{ij} refer to the i th row and the j th column of the matrix \mathbf{A} .

2.2 MLSVD

Definition 1: The casorati matrix is generalized by the n -mode unfoldings of a tensor. The 1-mode unfolding of tensor

$\mathcal{Y} \in \mathbb{R}^{N_x \times N_y \times N_z \times N_t}$ is represented as $\mathbf{Y}_{(1)} \in \mathbb{R}^{N_x \times N_y N_z N_t}$ where the columns are the information in x direction. Likewise, the 2-mode unfolding is $\mathbf{Y}_{(2)} \in \mathbb{R}^{N_y \times N_x N_z N_t}$, 3-mode unfolding is $\mathbf{Y}_{(3)} \in \mathbb{R}^{N_z \times N_x N_y N_t}$ and 4-mode unfolding is $\mathbf{Y}_{(4)} \in \mathbb{R}^{N_t \times N_x N_y N_z}$.

Definition 2: The 1-mode product of a matrix $\mathbf{U} \in \mathbb{R}^{J_x \times N_x}$ with $\mathcal{Y} \in \mathbb{R}^{N_x \times N_y \times N_z \times N_t}$ is a tensor with dimension $(J_x \times N_y \times N_z \times N_t)$ which has the entries

$$(\mathcal{Y} \times_1 \mathbf{U})_{j_x n_y n_z n_t} = \sum_{n_x} y_{n_x n_y n_z n_t} u_{j_x n_x}.$$

Likewise, the other n -mode multiplications are defined.

Definition 3: The scalar product between two tensors $\mathcal{Y}, \mathcal{Z} \in \mathbb{R}^{N_x \times N_y \times N_z \times N_t}$ is

$$\langle \mathcal{Y}, \mathcal{Z} \rangle = \sum_{n_x} \sum_{n_y} \sum_{n_z} \sum_{n_t} z_{n_x n_y n_z n_t}^* y_{n_x n_y n_z n_t},$$

where $*$ represents the complex conjugate.

Whenever the scalar product between two tensors is 0, they are orthogonal to each other. The Frobenius norm of a tensor is the square root of the scalar product of the tensor with itself, $\|\mathcal{Y}\|_F = \sqrt{\langle \mathcal{Y}, \mathcal{Y} \rangle}$.

Definition 4: The n -rank of \mathcal{Y} denoted by $R_n = \text{rank}_n(\mathcal{Y})$, is the dimension of the vector space spanned by the columns of the n -mode unfolding. The multilinear rank for \mathcal{Y} is represented as $\text{rank}_{\parallel}(\mathcal{Y}) = [R_x, R_y, R_z, R_t]$ where R_x, R_y, R_z, R_t are integers between 1 and N_x, N_y, N_z, N_t , respectively.

The MLSVD decomposes the data tensor $\mathcal{Y} \in \mathbb{R}^{N_x \times N_y \times N_z \times N_t}$ into

$$\mathcal{Y} = \mathcal{S} \times_1 \mathbf{U}^{(1)} \times_2 \mathbf{U}^{(2)} \times_3 \mathbf{U}^{(3)} \times_4 \mathbf{U}^{(4)},$$

where $\mathcal{S} \in \mathbb{R}^{N_x \times N_y \times N_z \times N_t}$ is an all-orthogonal tensor. An all-orthogonal tensor has the following properties. Let a subtensor be defined by fixing an n -mode index of \mathcal{S} . For example let the subtensor created by fixing the first mode value $n_x \in [1, \dots, N_x]$ to α be defined as $\mathcal{S}_{n_x=\alpha}$. This subtensor $\mathcal{S}_{n_x=\alpha}$ is orthogonal to any other $\mathcal{S}_{n_x=\beta}$ for all n_x, α and β given that $\alpha \neq \beta$. In addition, the frobenius norm of each subtensor is ordered, $\|\mathcal{S}_{n_x=1}\|_F \geq \|\mathcal{S}_{n_x=2}\|_F \dots \geq \|\mathcal{S}_{n_x=N_x}\|_F$. The matrices $\mathbf{U}^{(1)} \in \mathbb{R}^{N_x \times N_x}$, $\mathbf{U}^{(2)} \in \mathbb{R}^{N_y \times N_y}$, $\mathbf{U}^{(3)} \in \mathbb{R}^{N_z \times N_z}$ and $\mathbf{U}^{(4)} \in \mathbb{R}^{N_t \times N_t}$ are unitary.

3 SIGNAL MODEL

In nearly all commercial scanners the recordings are logarithmically compressed to deal with the large dynamic ranges. Here we model the logarithmically compressed DCEUS recordings as the addition of the original signal and the noise,

$$\mathcal{Y} = \mathcal{G} + \mathcal{E}, \quad (1)$$

where $\mathcal{G} \in \mathbb{R}^{N_x \times N_y \times N_z \times N_t}$ stands for the original signal, $\mathcal{Y} \in \mathbb{R}^{N_x \times N_y \times N_z \times N_t}$ stands for the received signal and $\mathcal{E} \in \mathbb{R}^{N_x \times N_y \times N_z \times N_t}$ stands for the noise. When only multiplicative noise is considered, and the logarithmic compression is applied, \mathcal{E} stands for the speckle noise (Barrois et al., 2013). After the logarithmic compression, speckle noise is shown to obey the Fisher-Tippet distribution, which can be approximated as a white Gaussian noise with outliers that has a fixed variance (Michailovich and Tannenbaum, 2006). There can be several other noise sources in practical scenarios, such as the motion artifacts due to the urologist's probe handling and the patient's breathing.

The time-intensity curves \mathcal{G} are assumed to follow the modified local density random walk (mLDRW)

model (Kuenen et al., 2011), which is given as

$$g_{xyz,t} = \alpha_{xyz} \sqrt{\frac{\kappa_{xyz}}{2\pi(t-t_0)}} e^{-\frac{\kappa_{xyz}(t-t_0-\mu_{xyz})^2}{2(t-t_0)}}. \quad (2)$$

Here, κ is the local dispersion-related parameter independent of the injection site's distance. For low values of dispersion, a symmetric curve and a high κ value are observed. This is expected to represent malignant regions (Mischi et al., 2009) (Kuenen et al., 2011). On the other hand, a low κ is expected to represent the benign regions.

4 PROPOSED ALGORITHM

The data tensor \mathcal{Y} is a 4D DCEUS recording where the first three are the spatial dimensions in the cartesian domain, and the fourth is the temporal dimension. We recover \mathcal{G} by truncating \mathcal{Y} with ranks $[R_x, R_y, R_z, R_t]$ that obey the condition $1 < R_x < N_x$, $1 < R_y < N_y$, $1 < R_z < N_z$ and $1 < R_t < N_t$. This assumption is expected to hold since the movement of the microbubbles is bounded by the spatial locations of the vascular architecture inside the prostate, and their temporal characteristics are a latent variable of indicator dilution models. In addition, we assume that the noise is independent of the signal itself. With these assumptions, the problem at hand transforms into a tensor rank estimation problem, where the rank that defines the signal subspace will be estimated, and the original signal will be recovered.

The multilinear truncation is done on each n -mode unfolding separately. This can be described as

$$\mathbf{Y}_{(1)} = \mathbf{U}^{(1)} \mathbf{\Sigma}^{(1)} \mathbf{V}^{(1)T} = \mathbf{\Sigma}^{(1)} \times_1 \mathbf{U}^{(1)} \times_2 \mathbf{V}^{(1)}$$

$$\mathbf{Y}_{(2)} = \mathbf{U}^{(2)} \mathbf{\Sigma}^{(2)} \mathbf{V}^{(2)T} = \mathbf{\Sigma}^{(2)} \times_1 \mathbf{U}^{(2)} \times_2 \mathbf{V}^{(2)}$$

$$\mathbf{Y}_{(3)} = \mathbf{U}^{(3)} \mathbf{\Sigma}^{(3)} \mathbf{V}^{(3)T} = \mathbf{\Sigma}^{(3)} \times_1 \mathbf{U}^{(3)} \times_2 \mathbf{V}^{(3)}$$

$$\mathbf{Y}_{(4)} = \mathbf{U}^{(4)} \mathbf{\Sigma}^{(4)} \mathbf{V}^{(4)T} = \mathbf{\Sigma}^{(4)} \times_1 \mathbf{U}^{(4)} \times_2 \mathbf{V}^{(4)}$$

Truncate each singular vector by first $R_i < N_i$ for $i \in [x, y, z, t]$. This can be described by the operation

$$\mathbf{Y}_{(i)} = \begin{bmatrix} \bar{\mathbf{U}}^{(i)} & \tilde{\mathbf{U}}^{(i)} \end{bmatrix} \begin{bmatrix} \mathbf{\Sigma}_{R_i}^{(i)} & \mathbf{0} \\ \mathbf{0} & \mathbf{\Sigma}_{N_i-R_i}^{(i)} \end{bmatrix} \begin{bmatrix} \tilde{\mathbf{V}}^{(i)T} \\ \bar{\mathbf{V}}^{(i)T} \end{bmatrix} \quad (3)$$

where $\bar{\mathbf{U}}^{(i)}$ is the column-wise stacking of first R_i vectors representing the eigenvectors of the highest singular values, $\tilde{\mathbf{U}}^{(i)}$ is the column-wise stacking of the $N_i - R_i$ columns that represent the eigenvectors of the rest of the singular values, $\tilde{\mathbf{V}}^{(i)T}$ and $\bar{\mathbf{V}}^{(i)T}$ are defined in a similar way but represent the right eigenvectors of the i th unfolding of \mathcal{Y} .

The multilinear ranks $rank_{\parallel} \mathcal{G}$ are estimated using the SCORE algorithm proposed by (Yokota et al., 2016). The truncation is done by projecting each mode to the column subspace represented by the estimated rank

$$\hat{\mathcal{G}} = \mathcal{Y} \times_1 \mathbf{U}^{(1)} \mathbf{U}^{(1)T} \times_2 \mathbf{U}^{(2)} \mathbf{U}^{(2)T} \times_3 \mathbf{U}^{(3)} \mathbf{U}^{(3)T} \times_4 \mathbf{U}^{(4)} \mathbf{U}^{(4)T}, \quad (4)$$

where $\hat{\mathcal{G}}$ represent the estimate of the TICs.

5 EXPERIMENTAL RESULTS

Two simulations and an in-vivo analysis are reported in section 5.1 and section 5.2, respectively. In section 5.1, a theoretical analysis is done to compare the performances of SVD and MLSVD for two noise scenarios. The TICs are generated according to the model described at (2). The speckle noise is added for the best-case scenario. Additionally, motion artifacts and white Gaussian noise are added for the worst-case scenario. The resulting signals are logarithmically compressed and then truncated using SVD and MLSVD. The ranks are estimated using two methods that are abbreviated as *mlsvd_min* and *mlsvd_score*. In the former, the rank that gives the least MSE is chosen and in the latter, the SCORE algorithm proposed by (Yokota et al., 2016) is used. The estimated signals are fit using the mLDRW model given at (2) using the algorithm described in (Kuenen et al., 2011) after reverting the logarithmic compression. For each algorithm, the mean squared error is calculated by

$$MSE = \frac{1}{N_x N_y N_z N_t} \sum_{x=1}^{N_x} \sum_{y=1}^{N_y} \sum_{z=1}^{N_z} \sum_{t=1}^{N_t} (\hat{g}_{xyzt} - g_{xyzt})^2. \quad (5)$$

5.1 Simulation

We consider a signal $\mathcal{G} \in \mathbb{R}^{10 \times 10 \times 10 \times 30}$ which holds TICs that obey the mLDRW model as described at (2). The voxel size is 0.75 mm, and the time step is 4 seconds. The simulated region holds three different TICs, which have the parameters that are commonly observed in the literature (Wildeboer et al., 2020), that is,

- $TIC_1(\kappa_1, \mu_1, \alpha_1) = [0.5 \pm 0.1, 30 \pm 1, 1000 \pm 10]$,
- $TIC_2(\kappa_2, \mu_2, \alpha_2) = [1 \pm 0.1, 25 \pm 1, 1600 \pm 10]$,
- $TIC_3(\kappa_3, \mu_3, \alpha_3) = [2 \pm 0.1, 15 \pm 1, 1200 \pm 10]$.

Let the first malignant region be defined as a $3 \times 3 \times 3$ block located at the indices $[x, y, z] = [2 : 5, 2 : 5, 2 : 5]$. The second malignant region is located at

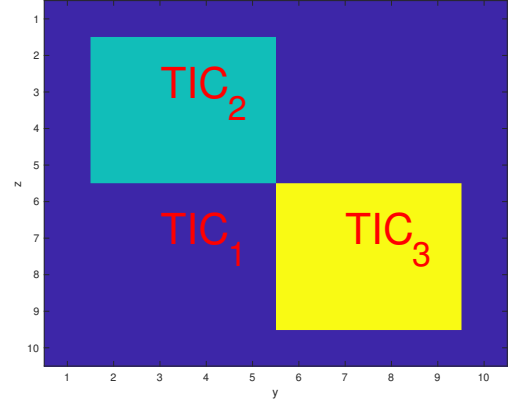


Figure 1: The simulation setup of 3D rectangular region with three different TICs. The slice at $x = 2$ is shown. Three different simulation areas where the dark blue (majority of the slice) represents the first region, the light blue (left top) rectangle represents the second region, and the yellow part (bottom right) represents the third region.

the indices $[x, y, z] = [2 : 5, 6 : 9, 6 : 9]$, and the benign region is the area that is not covered by the first two blocks. A slice at $x = 2$ represents these three different regions, which is given in Figure 1. The benign region (majority of the block) shown as dark blue is assigned as region 1, the light blue (left top) rectangle represents the region 2, and the yellow part (bottom right) represents the region 3. These numbers are used for referring to the malignant and benign regions. For example κ_1 will refer to the κ values inside the region 1, κ_2 for region 2 and κ_3 for region 3. The other parameters are represented in the same fashion. The true rank of the generated signal \mathcal{G} in this setup is $rank_{\parallel} \mathcal{G} = [2, 3, 3, 3]$.

Two noise scenarios are simulated. For Scenario 1, the TICs are noised with Rayleigh-shaped multiplicative noise. For Scenario 2, a variety of noise sources have been added. In addition to the multiplicative noise, we have added a sinusoidal breathing artifact with an amplitude of 0.5 mm and a frequency of 0.2 Hz, a random-walk displacement that has the maximum translation of 0.0125 mm at each step to simulate the probe-handling of the urologist, white Gaussian noise with 4 dB SNR where the SNR is calculated with respect to the averaged TICs. For each case, the error measures given at (5) is calculated and averaged across 100 Monte Carlo simulations. A plot of MSE can be observed in Figure 2 and Figure 4 for Scenario 1 and Scenario 2, respectively. Plot (a) show the MSE over 100 iterations when the highest 1 to 7 principal components are used for truncation. Since MLSVD does not share the same x axis, the MSE is drawn as a straight line on the same plot. The line with the circle markers is the average MSE over 100 iterations when the best performing trunca-

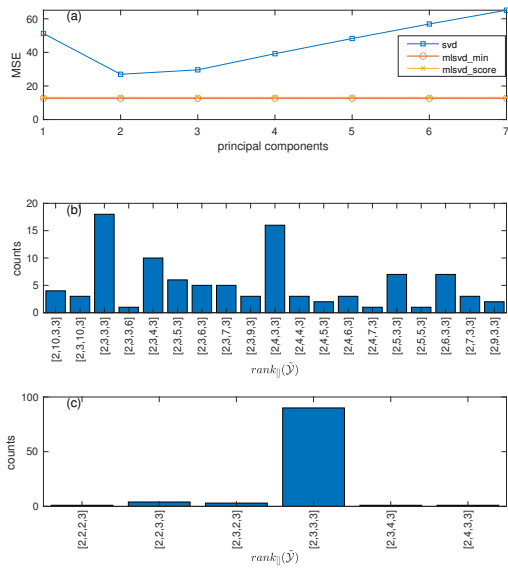


Figure 2: The performance comparison for Scenario 1. At (a), the MSE of SVD when several principal components are used to truncate is shown along with two lines that show the best performing MLSVD error over 100 iterations and the performance of MLSVD after the ranks are estimated with SCORE algorithm. At (b), the histogram of the ranks that gives the least MSE at each simulation is shown. At (c), the histogram of the ranks that are estimated with the SCORE algorithm is shown.

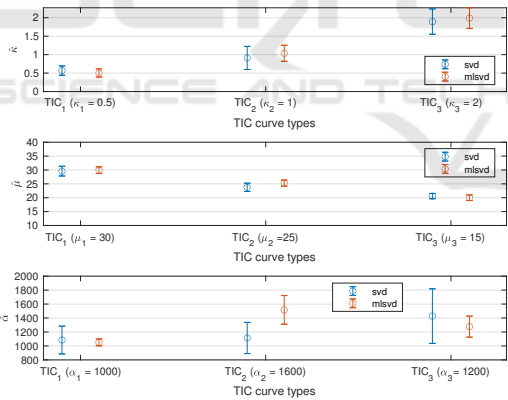


Figure 3: Plot that shows the mean and the standard deviation of the $\hat{\mu}$, $\hat{\kappa}$ and $\hat{\alpha}$ for three different TICs in Scenario 1. The circles represents the mean values whereas, the error bars represents the standard deviation. The mean and the standard deviation are calculated over 100 iterations.

tion is applied, and the line with cross markers is the MSE when the ranks are estimated using the SCORE algorithm. Plot (b) and (c) represent the histogram of the ranks that give the least MSE and the rank estimated by the SCORE algorithm, respectively. The estimated κ and μ parameters are shown in Figure 3 and Figure 5, respectively. In 87 percent of the cases, the correct rank is estimated by the SCORE algorithm,

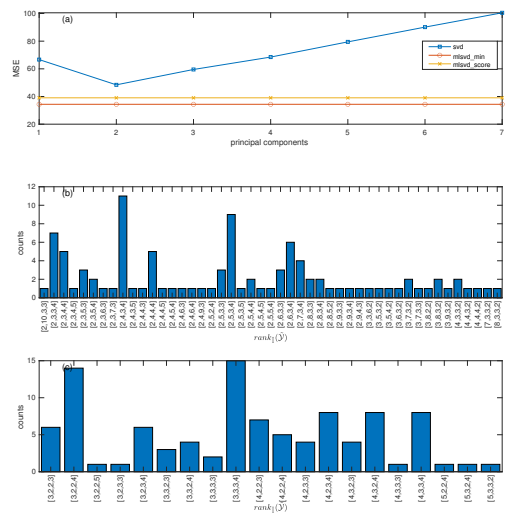


Figure 4: The performance comparison for Scenario 2. At (a), the MSE of SVD when several principal components are used to truncate is shown along with two lines that show the best performing MLSVD error over 100 iterations and the performance of MLSVD after the ranks are estimated with SCORE algorithm. At (b) the histogram of the ranks that gives the least MSE at each simulation are shown. At (c) the histogram of the ranks estimated with SCORE algorithm shown.

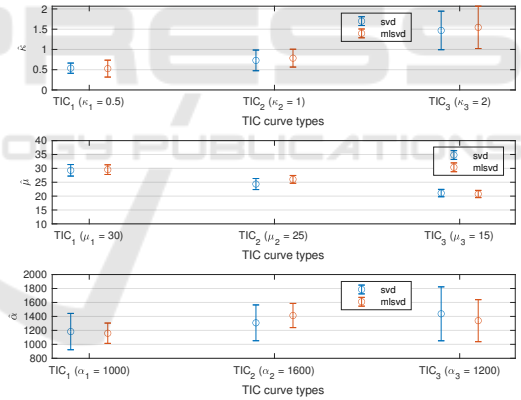


Figure 5: Plot that shows the mean and the standard deviation of the $\hat{\mu}$, $\hat{\kappa}$ and $\hat{\alpha}$ for three different TICs at Scenario 2. The circles represents the mean values whereas, the error bars represents the standard deviation. The mean and the standard deviation are calculated over 100 iterations.

which can be seen at plot (c) of Figure 2. For this case, the performance of *mlsvd_min* and *mlsvd_score* overlap suggesting that the SCORE algorithm gives the least mse over 100 iterations. Although a performance improvement over SVD is observed in Figure 4, the ranks are not estimated correctly when a variety of noise sources are added. The reasons are discussed at Section 6.

Table 1: The summary of simulation scenarios.

	$TIC_1(\kappa_1, \mu_1, \alpha_1)$	$TIC_2(\kappa_2, \mu_2, \alpha_2)$	$TIC_3(\kappa_3, \mu_3, \alpha_3)$	Number of Voxels TIC_1	Number of Voxels TIC_2	Number of Voxels TIC_3	Noise Types	Number of Simulations
Scenario 1	$(0.5 \pm 0.1, 30 \pm 1, 1000 \pm 10)$	$(1 \pm 0.1, 25 \pm 1, 1600 \pm 10)$	$(2 \pm 0.1, 15 \pm 1, 1200 \pm 10)$	872	64	64	Multiplicative	100
Scenario 2	$(0.5 \pm 0.1, 30 \pm 1, 1000 \pm 10)$	$(1 \pm 0.1, 25 \pm 1, 1600 \pm 10)$	$(2 \pm 0.1, 15 \pm 1, 1200 \pm 10)$	872	64	64	Multiplicative, Breathing, Motion, WGN	100

Table 2: The estimated model fit parameters across all patients.

	SVD		MLSVD-SCORE $\rho = 10e - 4$	
	Benign	Malignant	Benign	Malignant
κ	0.51 ($\sigma = 0.35$)	0.56 ($\sigma = 0.33$)	0.39 ($\sigma = 0.18$)	0.48 ($\sigma = 0.22$)
PV	94.73 ($\sigma = 29.57$)	104.05 ($\sigma = 27.53$)	87.87 ($\sigma = 26.33$)	98.49 ($\sigma = 24.03$)
PT	33.76 ($\sigma = 9.57$)	30.00 ($\sigma = 8.09$)	32.56 ($\sigma = 6.95$)	29.24 ($\sigma = 5.62$)
AT	15.12 ($\sigma = 4.96$)	13.72 ($\sigma = 4.23$)	14.32 ($\sigma = 3.44$)	13.41 ($\sigma = 3.11$)
WIT	18.64 ($\sigma = 9.41$)	16.28 ($\sigma = 7.44$)	18.24 ($\sigma = 5.91$)	15.84 ($\sigma = 4.08$)
μ	35.28 ($\sigma = 11.48$)	31.31 ($\sigma = 9.57$)	34.29 ($\sigma = 8.31$)	30.58 ($\sigma = 6.24$)
α	172.99 ($\sigma = 126.38$)	184.39 ($\sigma = 123.05$)	143.78 ($\sigma = 77.96$)	154.09 ($\sigma = 68.92$)

Table 3: The classification performance across all the patients.

	SVD	MLSVD-SCORE $(\rho = 10e - 4)$
$[\kappa_{sens}, \kappa_{spec}, \kappa_{AUC}, threshold]$	[0.54, 0.53, 0.57, 0.51]	[0.48, 0.65, 0.63 , 0.45]
$[P_{I_{sens}}, P_{I_{spec}}, P_{I_{AUC}}, threshold]$	[0.60, 0.54, 0.61, 99]	[0.63, 0.57, 0.64 , 93]
$[P_{T_{sens}}, P_{T_{spec}}, P_{T_{AUC}}, threshold]$	[0.57, 0.62, 0.61, 31]	[0.59, 0.65, 0.63 , 30]
$[\alpha_{sens}, \alpha_{spec}, \alpha_{AUC}, threshold]$	[0.54, 0.51, 0.55, 150]	[0.46, 0.64, 0.58 , 160]
$[WIT_{sens}, WIT_{spec}, WIT_{AUC}, threshold]$	[0.58, 0.59, 0.63, 6.6]	[0.62, 0.59, 0.66 , 5.7]
$[AT_{sens}, AT_{spec}, AT_{AUC}, threshold]$	[0.65, 0.58, 0.59 , 15]	[0.72, 0.59, 0.58, 13.8]
$[WIT_{sens}, WIT_{spec}, WIT_{AUC}, threshold]$	[0.58, 0.57, 0.56, 16]	[0.59, 0.58, 0.62 , 16.5]

5.2 In-vivo Analysis

The recording of 6 patients was acquired from the Second Affiliated Hospital of Zhejiang University (Hangzhou, Zhejiang, China). Written consent was obtained. A 2.4-mL bolus of SonoVue[®] was intravenously injected, and a 4D recording in contrast mode was obtained with a LOGIQ E9 scanner equipped with a RIC5-9-D endocavitary transducer driven at 4 MHz. The volume rate was fixed to 0.25 Hz by setting the image quality to low, and the disruption of microbubbles was avoided by fixing the mechanical index to 0.1. The patients went through prostatectomy after the recording. The prostate was sliced with 4-mm thickness, and for each slice, an annotation was made by the pathologist. The annotations were registered back to the domain of the recording, and the ground truth was obtained. Only two out of the six patients had significant lesions with Grade Group > 3. A region of interest is selected in the benign and malignant regions that are reasonably close to the true annotations. There are around 25000 voxels, of which 18000 are malignant.

The spatial resolution of the recording is regularized in space, and the data is downsampled by a factor of 3 as described by (Schalk et al., 2015b). The MLSVD is applied, and the signal is truncated using the ranks estimated by the SCORE (Yokota et al., 2016) algorithm where $\rho = 10e - 4$ is selected. The mLDRW model is fit as described at (Kuenen et al., 2011), and the perfusion and dispersion parameters

are extracted. The results can be seen in Table 2 and Table 3. In the former, the mean and the standard deviation of the features are shown. In the latter, the sensitivity, specificity, and area under the receiver operating characteristic curves are shown. The classification is done by determining the point in the receiver operating characteristic curve that is the closest to the upper left corner (sensitivity and specificity equal to 1) in Euclidean distance.

6 DISCUSSION

In this paper, the DCEUS sequences are denoised using SVD and MLSVD, and their performances are evaluated based on the quality of the TIC modeling. In section 5.1, two simulations are reported that employ the commonly observed noises in DCEUS recordings. The first simulation represents the best-case scenario where only speckle-noise exists. The second simulation represents the worst-case scenario where additive WGN and motion exist apart from the speckle noise. MLSVD mostly performs better at capturing the signal characteristics in both cases, providing a better estimate of dispersion and perfusion parameters. Both methods perform worse in the worst-case scenario and fail to estimate high κ values precisely. The low SNR might explain the decrease in performance.

The speckle noise can be modeled as a WGN with outliers (Michailovich and Tannenbaum, 2006), which results in the correct estimation of the rank for Scenario 1. The actual rank of the signal is $[2, 3, 3, 3]$, which is the same as the rank that is estimated the majority of the time. For this case, we can see in Figure 2 that the MSE of the best performing rank and the estimated rank overlap. In the cases where the rank was incorrectly estimated, the error is found to be within 15% of the MSE represented with the line *mlsvd_score*. The estimation of the correct rank fails for Scenario 2. Adding the other noise sources violates the WGN assumption and causes the rank estimator to perform poorly. This suggests that in a practical scenario where the recording suffers from various noise sources apart from the speckle noise, the proposed algorithm might not be suitable. In the figures Figure 2 and Figure 4, it can be observed that the best performing rank is not necessarily the true rank

of the data. The subfigures labeled with (b) in both plots suggest that the noise in some cases might occupy the highest ranks. For this reason, a higher rank might have provided a lower MSE.

Better classification performance of MLSVD over SVD is observed at Table 3. The improvement is more significant when a subset of the patients is considered. This might be due to the insignificant malignant voxels of the four patients that are investigated. The significant malignant lesions are expected to have a more distinct characteristic than benign tissue. This behavior is observed for two of the patients, who have significant lesions. The AUC is found to be greater than 0.8 for these two patients whereas, a similar performance has not been observed for the others.

7 CONCLUSION

In this paper, we proposed a denoising algorithm for detecting prostate cancer from 4D DCEUS recordings. Previously, SVD was proposed to denoise the single-dimensional TICs that suffer from low SNR. Here, we have retained the volumetric information by considering the tensor format of the recording and introduced an algorithm based on MLSVD and SCORE. The proposed algorithm is shown to outperform SVD in simulation and in in-vivo experiments. The in-vivo results have poor classification performance, which can be due to the insignificant lesions found in four of the six patients that have undergone prostatectomy. In future work, we plan to use a larger dataset and include other features used in the detection of angiogenesis.

ACKNOWLEDGEMENTS

This project is funded in part by Holland High Tech with a PPS supplement for research and development in the Topsector HTSM. We would like to acknowledge Prof. Pintong Huang for carrying out the clinical trials at the Second Affiliated Hospital of Zhejiang University (Hangzhou, Zhejiang, China).

REFERENCES

Bar-Zion, A. D., Tremblay-Darveau, C., Yin, M., Adam, D., and Foster, F. S. (2015). Denoising of contrast-enhanced ultrasound cine sequences based on a multiplicative model. *IEEE Transactions on Biomedical Engineering*, 62(8):1969–1980.

Barrois, G., Coron, A., Payen, T., Dizeux, A., and Bridal, L. (2013). A multiplicative model for improving microvascular flow estimation in dynamic contrast-enhanced ultrasound (dce-us): theory and experimental validation. *IEEE transactions on ultrasonics, ferroelectrics, and frequency control*, 60(11):2284–2294.

Bjaerum, S., Torp, H., and Kristoffersen, K. (2002). Clutter filter design for ultrasound color flow imaging. *IEEE Transactions on Ultrasonics, Ferroelectrics, and Frequency Control*, 49(2):204–216.

De Lathauwer, L., De Moor, B., and Vandewalle, J. (2000). A multilinear singular value decomposition. *SIAM journal on Matrix Analysis and Applications*, 21(4):1253–1278.

Delorme, S. and Knopp, M. (1998). Non-invasive vascular imaging: assessing tumour vascularity. *European radiology*, 8(4):517–527.

Eckersley, R. J., Sedelaar, J. M., Blomley, M. J., Wijkstra, H., deSouza, N. M., Cosgrove, D. O., and de la Rosette, J. J. (2002). Quantitative microbubble enhanced transrectal ultrasound as a tool for monitoring hormonal treatment of prostate carcinoma. *The Prostate*, 51(4):256–267.

Elie, N., Kaliski, A., Péronneau, P., Opolon, P., Roche, A., and Lassau, N. (2007). Methodology for quantifying interactions between perfusion evaluated by dceus and hypoxia throughout tumor growth. *Ultrasound in medicine & biology*, 33(4):549–560.

Elwenspoek, M. M. C., Sheppard, A. L., McInnes, M. D. F., Merriel, S. W. D., Rowe, E. W. J., Bryant, R. J., Donovan, J. L., and Whiting, P. (2019). Comparison of Multiparametric Magnetic Resonance Imaging and Targeted Biopsy With Systematic Biopsy Alone for the Diagnosis of Prostate Cancer: A Systematic Review and Meta-analysis. *JAMA Network Open*, 2(8):e198427–e198427.

Gillies, R. J., Schomack, P. A., Secomb, T. W., and Raghunand, N. (1999). Causes and effects of heterogeneous perfusion in tumors. *Neoplasia*, 1(3):197–207.

Joel, T. and Sivakumar, R. (2018). An extensive review on despeckling of medical ultrasound images using various transformation techniques. *Applied Acoustics*, 138:18–27.

Kuonen, M. P. J., Mischi, M., and Wijkstra, H. (2011). Contrast-ultrasound diffusion imaging for localization of prostate cancer. *IEEE Transactions on Medical Imaging*, 30(8):1493–1502.

Liu, G., Wu, S., and Huang, L. (2020). Contrast-enhanced ultrasound evaluation of the prostate before transrectal ultrasound-guided biopsy can improve diagnostic sensitivity: A star-d-compliant article. *Medicine*, 99(19).

Loeb, S., Vellekoop, A., Ahmed, H. U., Catto, J., Emberton, M., Nam, R., Rosario, D. J., Scattoni, V., and Lotan, Y. (2013). Systematic review of complications of prostate biopsy. *European Urology*, 64(6):876–892.

Michailovich, O. and Tannenbaum, A. (2006). Despeckling of medical ultrasound images. *IEEE Transactions on Ultrasonics, Ferroelectrics, and Frequency Control*, 53(1):64–78.

- Mischi, M., Kalker, A., and Korsten, H. (2003). Videodensitometric methods for cardiac output measurements. *EURASIP Journal on Applied Signal Processing*, 2003(5):479–489.
- Mischi, M., Kuennen, M., Wijkstra, H., Hendriks, A., and Korsten, H. (2009). Prostate cancer localization by contrast-ultrasound diffusion imaging. In *2009 IEEE International Ultrasonics Symposium*, pages 283–286.
- Mottet, N., Bellmunt, J., Bolla, M., Briers, E., Cumberbatch, M. G., De Santis, M., Fossati, N., Gross, T., Henry, A. M., Joniau, S., Lam, T. B., Mason, M. D., Matveev, V. B., Moldovan, P. C., van den Bergh, R. C., Van den Broeck, T., van der Poel, H. G., van der Kwast, T. H., Rouvière, O., Schoots, I. G., Wiegel, T., and Cornford, P. (2017). Eau-estro-siog guidelines on prostate cancer. part 1: Screening, diagnosis, and local treatment with curative intent. *European Urology*, 71(4):618–629.
- Ozgun, K. and Byram, B. (2020). A channel domain higher-order svd clutter rejection filter for small vessel ultrasound imaging. In *2020 IEEE International Ultrasonics Symposium (IUS)*, pages 1–4.
- Russo, G., Mischi, M., Scheepens, W., De la Rosette, J. J., and Wijkstra, H. (2012). Angiogenesis in prostate cancer: onset, progression and imaging. *BJU International*, 110(11c):E794–E808.
- Schalk, S. G., Demi, L., Smeenge, M., Mills, D. M., Wallace, K. D., de la Rosette, J. J. M. C. H., Wijkstra, H., and Mischi, M. (2015a). 4-d spatiotemporal analysis of ultrasound contrast agent dispersion for prostate cancer localization: a feasibility study. *IEEE Transactions on Ultrasonics, Ferroelectrics, and Frequency Control*, 62(5):839–851.
- Schalk, S. G., Demi, L., Smeenge, M., Mills, D. M., Wallace, K. D., de la Rosette, J. J. M. C. H., Wijkstra, H., and Mischi, M. (2015b). 4-d spatiotemporal analysis of ultrasound contrast agent dispersion for prostate cancer localization: a feasibility study. *IEEE Transactions on Ultrasonics, Ferroelectrics, and Frequency Control*, 62(5):839–851.
- Seitz, M., Shukla-Dave, A., Bjartell, A., Touijer, K., Sciarra, A., Bastian, P. J., Stief, C., Hricak, H., and Graser, A. (2009). Functional magnetic resonance imaging in prostate cancer. *European Urology*, 55(4):801–814.
- Siegel, R. L., Miller, K. D., Fuchs, H. E., and Jemal, A. (2021). Cancer statistics, 2021. *CA: A Cancer Journal for Clinicians*, 71(1):7–33.
- Strouthos, C., Lampaskis, M., Sboros, V., McNeilly, A., and Averkiou, M. (2010). Indicator dilution models for the quantification of microvascular blood flow with bolus administration of ultrasound contrast agents. *IEEE transactions on ultrasonics, ferroelectrics, and frequency control*, 57(6):1296–1310.
- Ukimura, O., Coleman, J. A., de la Taille, A., Emberton, M., Epstein, J. I., Freedland, S. J., Giannarini, G., Kibel, A. S., Montironi, R., Ploussard, G., Roobol, M. J., Scattoni, V., and Jones, J. S. (2013). Contemporary role of systematic prostate biopsies: Indications, techniques, and implications for patient care. *European Urology*, 63(2):214–230.
- Wildeboer, R., Van Sloun, R., Mannaerts, C., Van der Linden, J., Huang, P., Wijkstral, H., and Mischi, M. (2018a). Probabilistic 3d contrast-ultrasound tractography based on a convective-dispersion finite-element scheme. In *2018 IEEE International Ultrasonics Symposium (IUS)*, pages 1–9.
- Wildeboer, R. R., Sammali, F., van Sloun, R. J. G., Huang, Y., Chen, P., Bruce, M., Rabotti, C., Shulepov, S., Salomon, G., Schoot, B. C., Wijkstra, H., and Mischi, M. (2020). Blind source separation for clutter and noise suppression in ultrasound imaging: Review for different applications. *IEEE Transactions on Ultrasonics, Ferroelectrics, and Frequency Control*, 67(8):1497–1512.
- Wildeboer, R. R., van Sloun, R. J., Huang, P., Wijkstra, H., and Mischi, M. (2019). 3-d multi-parametric contrast-enhanced ultrasound for the prediction of prostate cancer. *Ultrasound in medicine & biology*, 45(10):2713–2724.
- Wildeboer, R. R., Van Sloun, R. J. G., Schalk, S. G., Mannaerts, C. K., Van Der Linden, J. C., Huang, P., Wijkstra, H., and Mischi, M. (2018b). Convective-dispersion modeling in 3d contrast-ultrasound imaging for the localization of prostate cancer. *IEEE Transactions on Medical Imaging*, 37(12):2593–2602.
- Yokota, T., Lee, N., and Cichocki, A. (2016). Robust multilinear tensor rank estimation using higher order singular value decomposition and information criteria. *IEEE Transactions on Signal Processing*, 65(5):1196–1206.
- Zhu, Y., Kim, M., Hoerig, C., and Insana, M. F. (2020). Experimental validation of perfusion imaging with hosvd clutter filters. *IEEE Transactions on Ultrasonics, Ferroelectrics, and Frequency Control*, 67(9):1830–1838.